

ARTICLE OPEN



Probing defect densities at the edges and inside Josephson junctions of superconducting qubits

Alexander Bilmes¹✉, Serhii Volosheniuk², Alexey V. Ustinov^{1,3,4} and Jürgen Lisenfeld¹

Tunneling defects in disordered materials form spurious two-level systems which are a major source of decoherence for micro-fabricated quantum devices. For superconducting qubits, defects in tunnel barriers of submicrometer-sized Josephson junctions couple strongest to the qubit, which necessitates optimization of the junction fabrication to mitigate defect formation. Here, we investigate whether defects appear predominantly at the edges or deep within the amorphous tunnel barrier of a junction. For this, we compare defect densities in differently shaped Al/AIO_x/Al Josephson junctions that are part of a Transmon qubit. We observe that the number of detectable junction-defects is proportional to the junction area, and does not significantly scale with the junction's circumference, which proposes that defects are evenly distributed inside the tunnel barrier. Moreover, we find very similar defect densities in thermally grown tunnel barriers that were formed either directly after the base electrode was deposited, or in a separate deposition step after removal of native oxide by Argon ion milling.

npj Quantum Information (2022)8:24; <https://doi.org/10.1038/s41534-022-00532-4>

INTRODUCTION

Microscopic tunneling defects forming parasitic two-level quantum systems^{1,2} have attracted much attention in the superconducting quantum computing community due to their detrimental influence on qubit coherence^{3–7}. Defects having an electric dipole moment may resonantly absorb energy from the oscillating electric field of the qubit mode, and efficiently dissipate it into the phonon⁸ or BCS quasiparticle bath⁹. This gives rise to a pronounced frequency-dependence of qubit energy relaxation times T_1 ^{10,11}, while strongly coupled defects which reside in the tunnel barrier of the Josephson junction may cause avoided level crossings in qubit spectroscopy^{4,12,13}. Moreover, the defect's resonance frequencies may show telegraphic switching or spectral diffusion^{14–16} due to their interaction¹⁷ with a bath of thermally activated defects, and this leads to resonance frequency fluctuations of qubits and resonators, and causes qubit dephasing^{18–23}.

Defects were found to reside at the interfaces and amorphous surface oxides of qubit electrodes^{24–26}, and they may emerge on substrates due to contaminants or processing damage^{27,28}. When defects are located inside the (typically amorphous) tunnel barrier of Josephson junctions, they couple most strongly to the qubit because of the concentrated electric field. Since the dawn of first superconducting qubits, the number of defects per junction was dramatically reduced by minimizing the junction area and thus the volume of the amorphous tunnel barrier²⁹. Nevertheless, Josephson junctions remain a vulnerability to up-scaled quantum processors, where individual qubits may spontaneously be spoiled by strongly coupled junction-defects drifting into qubit resonance³⁰. This necessitates further optimization of Josephson junctions.

Here, we investigate whether defects are predominantly formed at the edges of a tunnel junction or deep inside the tunnel barrier. This information shall support progress towards more coherent qubits by optimizing junction fabrication or geometry. Moreover, it can provide insights to the long-standing question about the

microscopic nature of the tunneling entities. For example, defects at the tunnel barrier edge might be formed by various species of adsorbates³¹ due to its exposure to processing chemicals and the atmosphere, while defects due to hydrogen-saturated dangling bonds³² could emerge all over the tunnel barrier due to hydrogen diffusibility in aluminum³³.

In a previous work³⁴, we have shown that defects in tunnel barriers of Transmon qubits can be distinguished from those at electrode interfaces by testing their response to an applied DC-electric field. This also revealed that qubits couple to a large number of defects residing in large-area “stray” Josephson junctions which appear as an artifact in standard shadow-evaporation^{35–38} or cross-junction^{29,39} techniques. Stray junctions should thus be avoided to maximize qubit coherence, e.g., by shorting them with a so-called bandage^{28,40,41}.

Here, we take advantage of stray Josephson junctions for studying defects, since their larger area results in a higher number of detectable defects which improves statistics. Meanwhile, sufficient qubit coherence can be preserved since the coupling to defects in the stray junction is reduced as most of the oscillating voltage drops across the much smaller qubit junction that is connected in series. Importantly, stray junctions are formed simultaneously with the small qubit junctions and thus are expected to have identical defect densities.

To analyze the amount of junction-defects as a function of the Josephson junction area and the length of its perimeter, we have fabricated a series of Xmon qubits¹¹ whose designs differ by the geometry of the large-area stray Josephson junctions. Figure 1a shows a sketch of the qubit island that is connected to ground via the stray junction in series to a small-junction dc-SQUID. The qubit electrodes were plasma-etched from a 100 nm-thick Al film, and the junctions were deposited with the shadow-evaporation technique after an electron-beam lithography step. Finally, Al bandages were deposited which either short the stray junction (see reference qubit in Fig. 1c) or connect it to the qubit island

¹Physikalisches Institut, Karlsruhe Institute of Technology, 76131 Karlsruhe, Germany. ²Kavli Institute of Nanoscience, Delft University of Technology, 2628 CJ Delft, The Netherlands. ³Russian Quantum Center, Skolkovo, Moscow 143025, Russia. ⁴National University of Science and Technology “MISIS”, 119049 Moscow, Russia.

✉email: alexander.bilmes@kit.edu

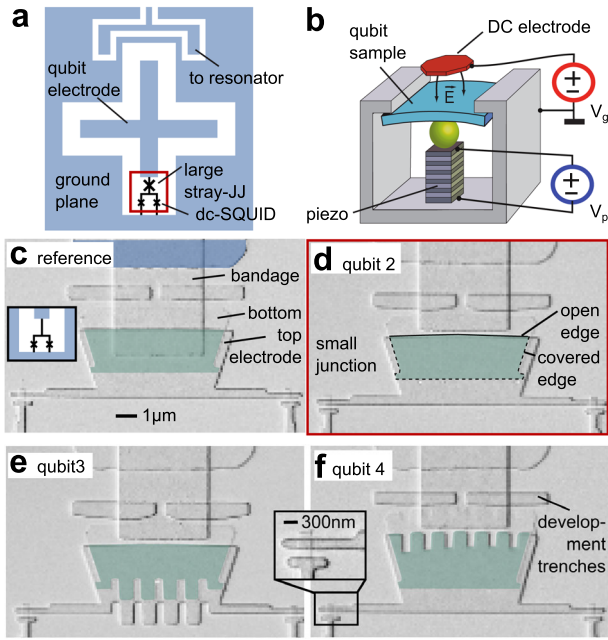


Fig. 1 Qubits with varying junction geometry. **a** Sketch of the qubit electrode that is connected to ground via a large area (“stray”) junction in series with a pair of small junctions. **b** Setup used to tune defects by an electric field from a voltage-biased electrode, and by mechanical strain from a piezo actuator bending the chip. **c–f** Photographs of large-area junctions (scale bar denotes 1 μm) with different geometries on the same qubit chip. The stray junction area is highlighted in dark cyan. **c** Reference qubit, where the stray junction is shorted using a bandage layer⁵¹. **d** Stray junction with the smallest edge length. The black solid and dashed lines indicate the junction edges that are exposed to air and covered by the top electrode metal, respectively. **e** and **f** Stray junctions with either the open or covered edge elongated by a tooth pattern. The development trenches are explained in the Supplementary Methods I. The inset in **f** shows a zoom onto a small Josephson junction. The small junction dimensions are on average 260 nm \times 280 nm.

(see Fig. 1d–f). Fabrication details are given in Supplementary Methods I.

We aim to compare the concentration of defects inside the tunnel barrier with those emerging at junction edges. Moreover, we distinguish two types of junction edges: the “covered edge” that is capped by the junction’s top electrode, and the “open edge” that is exposed to air (see Fig. 1d). While the area A_S of each stray junction was designed to be roughly the same, the length of either the covered (l_{cov}) or open (l_{op}) edge was extended by a tooth-shape pattern as shown in Fig. 1e, f, respectively. Table 1 summarizes the parameters of the qubits that were fabricated on two chips.

The standard tunneling model^{2,42} describes a defect by the two lowest energy eigenstates in a double-well potential, whose transition energy is $E = \sqrt{\Delta^2 + \varepsilon^2}$. Here, Δ is the constant tunnel energy, and $\varepsilon = \varepsilon_i + 2\mathbf{p}\mathbf{F} + 2\boldsymbol{\gamma}\mathbf{S}$ is the asymmetry energy given by an intrinsic offset ε_i and the local strengths of electric field \mathbf{F} and strain \mathbf{S} , where \mathbf{p} is the defect’s electric dipole moment, and $\boldsymbol{\gamma}$ is its deformation potential. As described elsewhere³⁴, our setup (see Fig. 1b) provides in-situ control of the mechanical strain in the sample and the ability to apply a global DC-electric field, both of which can be used to tune the defect’s resonance frequencies. For this work, we test the defects’ response to an applied electric field to distinguish whether they are located in the tunnel barrier of a Josephson junction or at a circuit interface. Since DC-electric fields inside the tunnel barrier are negligible for a qubit in the Transmon

regime⁴³, junction-defects are identified by their vanishing response to the applied E-field⁴⁴.

RESULTS

Data acquisition

To detect defects, we employ the swap-spectroscopy protocol^{17,45,46} for a rapid estimate of the qubit’s energy relaxation time T_1 in dependence of frequency. In such data, Lorentzian dips in T_1 reveal the frequencies at which defects are resonant with the qubit¹¹. We repeat such measurements for a range of applied electric field and mechanical strain and alternate between both tuning channels to characterize the responses of each visible defect. Here, strain-tuning is used to sort out eventual parasitic circuit modes which show no strain response, and to increase the number of detectable defects. Figure 2 shows extracts of resulting data sets, where some exemplary traces of junction-defects are highlighted in blue color, while red color marks traces of field-tunable defects residing on electrode interfaces. The yellow traces indicate non-classified defects whose location could not be identified since they were observed only during strain sweeps (blue framed data segments).

We then obtain a measure for the spectral density of detected junction-defects $\tilde{\rho}_{JJ}$ by normalizing the average number of observed junction-defect traces at each applied strain to the investigated frequency range which is typically 1 GHz (see Supplementary Methods II for further details). Table 1 summarizes the extracted $\tilde{\rho}_{JJ}$ values and that of non-junction defects $\tilde{\rho}_{surf}$ (“surface-defects”) detected on two sample chips.

The so-called shadow-junctions on chip 1 were formed using the shadow evaporation Dolan technique³⁶, where the bottom electrode is deposited, oxidized, and capped by the top electrode without removing the chip from the deposition chamber. The junctions on chip 2 were formed using the same type resist mask and identical design, however the junction’s bottom electrode was exposed to air intentionally, which required Argon-milling⁴⁷ to remove the native oxide before tunnel barrier growth. This process applied to chip 2 shall emulate so-called cross-type junctions^{29,39} whose electrodes are made in different lithography steps. In the reference qubits 1.1 and 2.1, which have no stray junctions, only few junction-defects were detected. This is an explicit verification that stray junctions increase the amount of detrimental defects coupled to the qubit, and a further affirmation that they should be omitted³⁴.

Junction-defects

The defect spectral density $\tilde{\rho}_{SJ}$ in stray junctions is expected to be proportional to junction dimensions:

$$\tilde{\rho}_{SJ} = \rho_A A_S + \rho_{op} l_{op} d + \rho_{cov} l_{cov} d, \quad (1)$$

where A_S , and l_{op} and l_{cov} are the respective stray junction area, and length of the open and the covered stray junction edges. The respective defect densities per GHz and per unit area are denoted by ρ_A , ρ_{op} , and ρ_{cov} . For the effective width of the edge, we take $d \sim 2$ nm as discussed later. The values $\tilde{\rho}_{SJ}$ are obtained by subtracting from $\tilde{\rho}_{JJ}$ (quoted in Table 1) the defect density inside of the small fixed-size junctions of reference qubits on the respective sample chip. The best-fitting values to Eq. (1) are

$$\begin{aligned} \rho_A &= (1.5 \pm 0.3) (\text{GHz} \cdot \mu\text{m}^2)^{-1} \\ \rho_{op} &= (3 \pm 106) (\text{GHz} \cdot \mu\text{m}^2)^{-1} \\ \rho_{cov} &= (62 \pm 114) (\text{GHz} \cdot \mu\text{m}^2)^{-1} \end{aligned} \quad (2)$$

from which we deduce the relative share of defects at open and covered edges in large junctions to be on average $(0.3 \pm 9.1)\%$ and $(7.5 \pm 13.6)\%$, respectively. This, and the fact that only the fit value of ρ_A exceeds its fit uncertainty suggest that $\tilde{\rho}_{SJ}$ predominantly

Table 1. Qubit parameters and defect statistics.

chip&qubit No.	$A_S \mu\text{m}^2$	$l_{op} \mu\text{m}$	$l_{cov} \mu\text{m}$	$\tilde{\rho}_{JJ} 1/\text{GHz}$	$\tilde{\rho}_{surf} 1/\text{GHz}$	$\tilde{\rho}_0 1/\text{GHz}$	$f_{01} \text{GHz}$	$T_1 \mu\text{s}$
1.1	–	–	–	0.8	28.8	7.7	6.0	10
1.2	12.1	7.1	10.1	19.6	10.0	3.5	6.0	10
1.3	12.7	7.1	19.1	19.6	10.2	3.0	6.2	6
1.4	14.0	15.7	11.1	22.5	24.7	9.7	6.2	8
2.1	–	–	–	2.3	67.7	7.1	5.9	17
2.2	13.1	6.6	10.8	22.4	22.4	3.3	5.8	11
2.3	13.6	6.6	18.4	23.8	23.8	3.9	5.7	12
2.4	14.3	17.2	11.7	25.4	64.9	7.1	5.9	8

Chip 1 contains shadow-junctions made with Dolan bridges, while chip 2 contains cross-type junctions employing intermediate Ar ion milling. A_S denotes the stray junction area. l_{op} and l_{cov} are the lengths of the open and covered stray junction edges, respectively. $\tilde{\rho}_{JJ}$ is the measured spectral density of junction-defects, $\tilde{\rho}_{surf}$ that of defects on electrode surfaces, and $\tilde{\rho}_0$ that of unclassified defects. f_{01} denotes the qubit's maximum resonance frequency, and T_1 is their average energy relaxation time. The qubit charge energy is $E_C = 0.2 \text{ GHz} \cdot h$, and the Josephson energies E_J are $24 \text{ GHz} \cdot h$ and $21 \text{ GHz} \cdot h$ for samples 1 and 2, respectively. The average vacuum fluctuation strength of the qubit plasma oscillation field is $2.3 \text{ kV} \cdot \text{m}^{-1}$ in the small junction, and $25 \text{ V} \cdot \text{m}^{-1}$ in the stray junction. In total 580 defects were detected on qubit surfaces, and 420 inside the Josephson junctions.

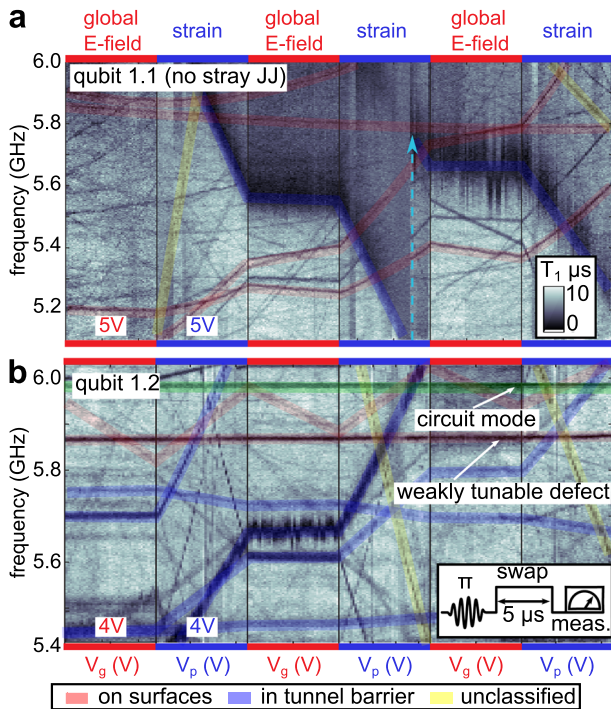


Fig. 2 Spectroscopy of defect resonance frequencies in dependence of the applied global electric field (segments with red borders) and the mechanical strain (blue frames). Dark traces indicate reduced qubit T_1 time due to resonance with a defect. The colored shadings indicate defect locations listed in the legend. Note that in **a**, a defect in the small junction is observed, whose large coupling strength affects the qubit coherence in a wide band. Apparently, a shift of its asymmetry energy occurred during measurement (see dashed arrow), which illustrates how defects can spontaneously (dis)appear in the qubit's spectrum. The strain-tunability statistics of defects detected in Josephson junctions are analyzed in another work⁵².

scales with the junction area, as similarly reported in previous works^{4,5,48} on large-area Josephson junctions. We note that more data is required to estimate the share of junction-defects that reside at tunnel barrier edges ("edge-defects") of small junctions, as explained in more details in Supplementary Discussion I.

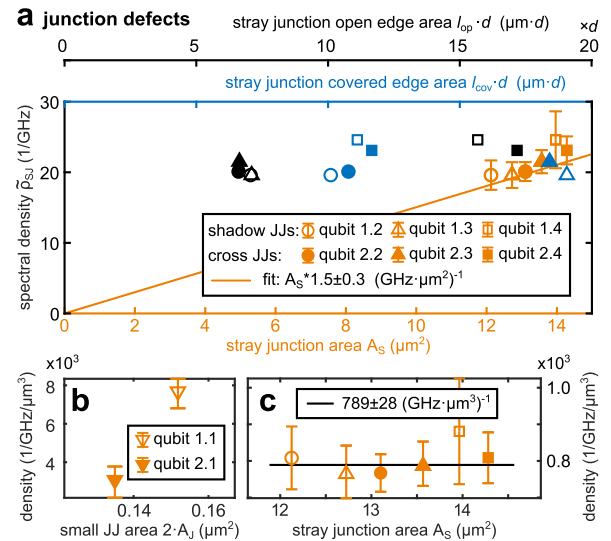


Fig. 3 Densities of defects in stray junctions of various shapes, each embedded in a Transmon qubit circuit. **a** Spectral density $\tilde{\rho}_{SJ}$ of detectable defects which reside in the stray junction, plotted vs. the stray junction area (orange), or the open (black) or covered (blue) stray junction edge area (edge length times the effective edge width). The linear fit of Eq. (1) returns the spectral defect density per junction area inside the AlO_x tunnel barrier (the slope of the orange line). **b** The density of detectable defects in the small junction of the reference qubits 1.1 and 1.2, which is larger than the defect density in the stray junctions (see **c**) because of the stronger electric field. **c** Volume defect density $\tilde{\rho}_{SJ}/(A_S d)$ which is constant for all investigated stray junctions, in agreement to the fitted slope shown in **a**.

The key contribution of the junction area to $\tilde{\rho}_{SJ}$ is further illustrated in Fig. 3a where the orange line represents the linear fit reported in Eq. (2) (see further details in Supplementary Discussion I). The error bar $\tilde{\rho}_0 \tilde{\rho}_{SJ} / (\tilde{\rho}_{SJ} + \tilde{\rho}_{surf})$ is the spectral density of non-classified detected defects $\tilde{\rho}_0$ multiplied with the relative part of junction-defects. Assuming a tunnel barrier thickness of 2 nm, the slope of the linear fit indicates a junction-defect density of $\sim 760 (\text{GHz} \cdot \mu\text{m}^3)^{-1}$. This value is confirmed by the data in Fig. 3c, where the volume density is calculated directly from the data points of Fig. 3a and the corresponding stray junction areas. As a note, in Fig. 3b we see that the spatial density of detectable defects in the small junction is significantly larger than in the stray junctions. This is expected due to the stronger electric field inside

the small junction, which enables one to detect also defects having smaller effective dipole moments.

As a note, we applied the fit of Eq. (2) to merged data from both chips, since we detected the same volume density of defects (see Fig. 3c) in both junction types. This observation indicates that dielectric losses are comparable in Josephson junctions patterned using either the shadow^{35–38} or the cross-junction^{29,39} techniques.

Surface-defects

Detectable surface-defects are concentrated at film edges of the qubit electrodes, and it requires special methods to distinguish at which interface they reside^{25,26}. However, the here-developed stray junction architecture allows one to independently assess densities of defects which reside at the substrate-metal and metal-air interface along the covered and open junction edges, respectively. A fit of $\tilde{\rho}_{\text{surf}}$ data quoted in Table 1 to a linear function $\rho_{\text{op}}^{\text{surf}} l_{\text{op}} + \rho_{\text{cov}}^{\text{surf}} l_{\text{cov}} + \text{const}$ suggests that, compared to the metal-air interface at the junction's open edge, fewer defects reside at the substrate-metal interface along the covered junction edge (see Supplementary Discussion II for more details), which is in accordance with our previous findings²⁶. Here, $\rho_{\text{op}}^{\text{surf}}$ and $\rho_{\text{cov}}^{\text{surf}}$ are respective defect densities along the open and covered junction edge, and the offset is due to surface-defects on qubit electrodes.

Discussion of defect locations

The distribution of DC-electric fields generated by the DC-gate was simulated using the ANSYS finite element solver, to test whether edge-defects are exposed to the applied E-field. Figure 4a contains a simplified sketch of a Josephson junction's profile, where the black continuous and black dashed squares indicate the cross-sections of the covered and open junction edges, respectively. The region emphasized with a red square is magnified in Fig. 4b, showing the field distribution at the open junction edge when 1 V is applied to the DC-gate. The DC-potential of the top

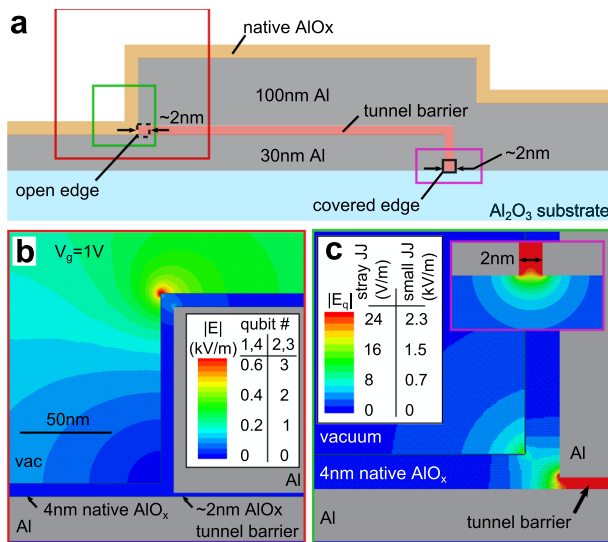


Fig. 4 Electric field distribution near the edges of a Josephson junction, obtained with finite element simulations. **a** Sketch of the junction's cross-section (not to scale). **b** Electric field strength (color-coded) generated by the DC-gate electrode near the open edge of the junction. The legend distinguishes between qubits due to their different positions relative to the gate electrode. We see that the open edge is screened by the junction's top electrode so that defects residing there are not field-tunable and cannot be confused with surface-defects. **c** Strength of the electric field induced by the qubit plasma oscillations at the open and covered (see inset) edges. The color bar indicates field strengths in the small and stray junctions.

and bottom junction electrodes were set to zero as it is the case for Xmon (i.e. grounded Transmon) qubits.

As visible in Fig. 4b, the ~ 10 nm wide region around the open edge is free of applied DC-electric fields due to screening by the junction's top electrode. For the same reason, the applied DC fields are zero at the covered edge. We thus can be sure that edge-defects are not field-tunable, and cannot be confused with surface-defects. Note that each qubit on the same chip couples differently to the DC-gate electrode, which is captured in the legend of Fig. 4b.

The AC-electric field strength induced by the qubit plasma oscillation at the open junction edge is shown in Fig. 4c where the inset shows the qubit field at the covered edge, and the legend indicates the field strengths in the small and the stray junctions. One recognizes that the qubit field is strongly confined in the tunnel barrier, and decays very fast outside, on a length scale of the tunnel barrier thickness $d \sim 2$ nm. This means that surface-defects which reside within a distance range of ca. 2–10 nm to the open edges of the stray junctions (where they are not field-tunable), as well as defects which reside at the substrate-metal interface close to the stray junction's covered edge, don't couple to the qubit, and cannot be confused with edge-defects. This is not necessarily the case at the small junctions' edges where the qubit fields are significantly larger. However, the contribution of the small junctions to the measured junction-defect density is only a small offset as mentioned before.

DISCUSSION

We have studied densities of microscopic material defects in Josephson junctions of various shapes using superconducting Transmon qubits. We observed that in $\sim 13 \mu\text{m}^2$ large Al/AIO_x/Al Josephson junctions fabricated using shadow evaporation and thermal tunnel barrier growth, the total amount of detectable junction-defects does not significantly scale with the junction edge lengths which were varied by a factor of two, but with the junction area.

Thus, relevant defects seem to be evenly distributed all over the tunnel barrier of the Josephson contact, which supports the old-standing strategy to reduce the dielectric losses of a Josephson junction by minimizing its footprint. We note that the size of our data set acquired on large junctions does not allow us to predict the relative share of edge defects in submicron-sized junctions. This possibly could be investigated using the here-reported method applied to large-area and high aspect-ratio Josephson junctions⁴⁹ where the effect of junction edges is amplified like in small junctions, while the advantage of good defect statistics is preserved.

As an outlook, we emphasize that the here-presented technique to study junction-defects in large-area stray Josephson junctions is also suitable to study how the defect density and qubit coherence scale with the tunnel barrier thickness, which is another open question on the way to improved junctions.

We further observe that AlO_x tunnel barriers, which were thermally created A in-situ after deposition of the bottom junction electrode, and B after application of Argon-milling to the bottom electrode, show the same density of detectable defects. This indicates that relevant defects are formed due to structural disorder rather than contamination from the Argon plasma, like implanted Argon ions and re-deposited mask and substrate residuals. This confirms that shadow^{35–38} and cross junctions^{29,39} are equally suitable for high-coherence qubits^{39,50}.

As a note, we observe that the density of surface-defects scales only with the open edge length of the large-area junction. This indicates that the interface of aluminum to the sapphire substrate does not notably contribute to the amount of detectable defects, which is in agreement with our previous studies^{25,26}, and leaves room for speculations. For example, defects at the substrate-metal

interface might be screened by the superconducting condensate⁹, while at the metal–air interface defects are separated from the metal by the native Al oxide.

METHODS

Sample fabrication

The Transmon electrodes and the readout circuitry were patterned into a 100 nm thick Aluminum groundplane in an inductively coupled plasma device, using an S1805 optical resist mask. The small and the stray Josephson junctions were simultaneously deposited in a thermal evaporation PLASSYS device using a double-resist mask patterned by eBeam-lithography. The bottom junction electrode consisted 30 nm thick Al which was deposited at an angle of 50°, and at a rate of 1 nm/s. For sample #1, the 100 nm thick Aluminum top electrode was deposited without breaking vacuum at the same rate but at zero tilt, after creation of the AlO_x tunnel barrier (static oxidation, exposure of 1100 s · mBar). The junctions on sample #2 were made using the same design and type of resist mask, however the bottom electrode was exposed to air after deposition of the bottom electrode, so that an Argon milling step was required to clean off the oxide from the bottom electrode prior thermal growth of the tunnel barrier and the successive deposition of the top electrode. After lift-off of the junction layers, a further electron-beam lithography step was applied, and aluminum bandages were placed to selectively either contact or short the stray junction. See Supplementary Methods I for further details.

Supplementary methods and discussion

In Supplementary Methods II, the detection and counting method of defects is presented and additional raw data plots like in Fig. 2 are shown. Supplementary Discussion I and II contain additional analysis of defect densities in junctions and at other qubit interfaces.

DATA AVAILABILITY

Data is available upon reasonable request.

CODE AVAILABILITY

Code is available upon reasonable request.

Received: 7 August 2021; Accepted: 11 January 2022;

Published online: 07 March 2022

REFERENCES

- Phillips, W. A. Two-level states in glasses. *Rep. Prog. Phys.* **50**, 1657 (1987).
- Anderson, P. W., Halperin, B. I. & Varma, C. M. Anomalous low-temperature thermal properties of glasses and spin glasses. *Philos. Mag.* **25**, 1–9 (1972).
- Müller, C., Cole, J. H. & Lisenfeld, J. Towards understanding two-level-systems in amorphous solids: insights from quantum circuits. *Rep. Prog. Phys.* **82**, 124501 (2019).
- Martinis, J. M. et al. Decoherence in Josephson qubits from dielectric loss. *Phys. Rev. Lett.* **95**, 210503 (2005).
- Stoutimore, M. J. A., Khalil, M. S., Lobb, C. J. & Osborn, K. D. A Josephson junction defect spectrometer for measuring two-level systems. *Appl. Phys. Lett.* **101**, 062602 (2012).
- Stoutimore, M. J. A., Khalil, M. S., Lobb, C. J. & Osborn, K. D. A Josephson junction defect spectrometer for measuring two-level systems. *Appl. Phys. Lett.* **101**, 062602 (2012).
- McRae, C. R. H. et al. Materials loss measurements using superconducting microwave resonators. *Rev. Sci. Instrum.* **91**, 091101 (2020).
- Jäckle, J. On the ultrasonic attenuation in glasses at low temperatures. *Z. Phys. A Hadrons Nuclei* **257**, 212–223 (1972).
- Bilmes, A. et al. Electronic decoherence of two-level systems in a Josephson junction. *Phys. Rev. B* **96**, 064504 (2017).
- Kim, Z. et al. Anomalous avoided level crossings in a Cooper-pair box spectrum. *Phys. Rev. B* **78**, 144506 (2008).
- Barends, R. et al. Coherent Josephson qubit suitable for scalable quantum integrated circuits. *Phys. Rev. Lett.* **111**, 080502 (2013).

- Lupascu, A., Bertet, P., Driessen, E. F. C., Harmans, C. J. P. M. & Mooij, J. E. One- and two-photon spectroscopy of a flux qubit coupled to a microscopic defect. *Phys. Rev. B* **80**, 172506 (2008).
- Palomaki, T. et al. Multilevel spectroscopy of two-level systems coupled to a dc squid phase qubit. *Phys. Rev. B* **81**, 144503 (2010).
- Schlör, S. et al. Correlating decoherence in transmon qubits: Low frequency noise by single fluctuators. *Phys. Rev. Lett.* **123**, 190502 (2019).
- Klimov, P. V. et al. Fluctuations of energy-relaxation times in superconducting qubits. *Phys. Rev. Lett.* **121**, 090502 (2018).
- Burnett, J. J. et al. Decoherence benchmarking of superconducting qubits. *NPJ Quantum Inform.* **5**, 54 (2019).
- Lisenfeld, J. et al. Observation of directly interacting coherent two-level systems in an amorphous material. *Nat. Commun.* **6**, 6182 (2015).
- Müller, C., Lisenfeld, J., Shnirman, A. & Poletto, S. Interacting two-level defects as sources of fluctuating high-frequency noise in superconducting circuits. *Phys. Rev. B* **92**, 035442 (2015).
- Paladino, E., Galperin, Y. M., Falci, G. & Altshuler, B. L. $1/f$ noise: Implications for solid-state quantum information. *Rev. Mod. Phys.* **86**, 361–418 (2014).
- Burin, A. L., Matiyahu, S. & Schechter, M. Low-temperature $1/f$ noise in microwave dielectric constant of amorphous dielectrics in Josephson qubits. *Phys. Rev. B* **92**, 174201 (2015).
- Faoro, L. & Ioffe, L. B. Interacting tunneling model for two-level systems in amorphous materials and its predictions for their dephasing and noise in superconducting microresonators. *Phys. Rev. B* **91**, 014201 (2015).
- Meißner, S. M., Seiler, A., Lisenfeld, J., Ustinov, A. V. & Weiss, G. Probing individual tunneling fluctuators with coherently controlled tunneling systems. *Phys. Rev. B* **97**, 180505 (2018).
- de Graaf, S. E., Mahashabde, S., Kubatkin, S. E., Tzalenchuk, A. Y. & Danilov, A. V. Quantifying dynamics and interactions of individual spurious low-energy fluctuators in superconducting circuits. *Phys. Rev. B* **103**, 174103 (2021).
- Wang, C. et al. Surface participation and dielectric loss in superconducting qubits. *Appl. Phys. Lett.* **107** (2015).
- Bilmes, A. *Resolving Locations of Defects in Superconducting Transmon Qubits*, dissertation, Karlsruhe Institute of Technology (KIT) (2019) <https://doi.org/10.5445/KSP/1000097557>.
- Bilmes, A. et al. Resolving the positions of defects in superconducting quantum bits. *Sci. Rep.* **10**, 1–6 (2020).
- Quintana, C. M. et al. Characterization and reduction of microfabrication-induced decoherence in superconducting quantum circuits. *Appl. Phys. Lett.* **105**, 062601 (2014).
- Dunsworth, A. et al. Characterization and reduction of capacitive loss induced by sub-micron Josephson junction fabrication in superconducting qubits. *Appl. Phys. Lett.* **111**, 022601 (2017).
- Steffen, M. et al. State tomography of capacitively shunted phase qubits with high fidelity. *Phys. Rev. Lett.* **97**, 050502 (2006).
- Klimov, P. Operating a quantum processor with material defects. V35.00013 (APS March Meeting, 2019).
- de Graaf, S. E. et al. Direct identification of dilute surface spins on Al₂O₃: origin of flux noise in quantum circuits. *Phys. Rev. Lett.* **118**, 057703 (2017).
- Holder, A. M., Osborn, K. D., Lobb, C. & Musgrave, C. B. Bulk and surface tunneling hydrogen defects in alumina. *Phys. Rev. Lett.* **111**, 065901 (2013).
- Li, M. et al. Effect of hydrogen on the integrity of aluminium-oxide interface at elevated temperatures. *Nat. Commun.* **8**, 14564 (2017).
- Lisenfeld, J. et al. Electric field spectroscopy of material defects in transmon qubits. *NPJ Quantum Inform.* **5**, 1–6 (2019).
- Niemeyer, J. & Kose, V. Observation of large dc supercurrents at nonzero voltages in Josephson tunnel junctions. *Appl. Phys. Lett.* **29**, 380–382 (1976).
- Dolan, G. J. Offset masks for lift-off photoprocessing. *Appl. Phys. Lett.* **31**, 337–339 (1977).
- Potts, A., Parker, G., Baumberg, J. & de Groot, P. CMOS compatible fabrication methods for submicron Josephson junction qubits. *IEE Proc Sci. Meas. Technol.* **148**, 225–228 (2001).
- Lecocq, F. et al. Junction fabrication by shadow evaporation without a suspended bridge. *Nanotechnology* **22**, 315302 (2011).
- Wu, X. et al. Overlap junctions for high coherence superconducting qubits. *Appl. Phys. Lett.* **111**, 032602 (2017).
- Osman, A. et al. Simplified Josephson-junction fabrication process for reproducibly high-performance superconducting qubits. *Appl. Phys. Lett.* **118**, 064002 (2021).
- Bilmes, A., Händel, A. K., Volosheniuk, S., Ustinov, A. V. & Lisenfeld, J. In-situ bandaged Josephson junctions for superconducting quantum processors. *Supercond. Sci. Technol.* **34**, 125011 (2021).
- Phillips, W. A. Tunneling states in amorphous solids. *J. Low Temp. Phys.* **7**, 351 (1972).

43. Koch, J. et al. Charge-insensitive qubit design derived from the cooper pair box. *Phys. Rev. A* **76**, 042319 (2007).
44. Bilmes, A., Volosheniuk, S., Brehm, J. D., Ustinov, A. V. & Lisenfeld, J. Quantum sensors for microscopic tunneling systems. *NPJ Quantum Inform.* **7**, 27 (2021).
45. Cooper, K. B. et al. Observation of quantum oscillations between a josephson phase qubit and a microscopic resonator using fast readout. *Phys. Rev. Lett.* **93**, 180401 (2004).
46. Shalibo, Y. et al. Lifetime and coherence of two-level defects in a Josephson junction. *Phys. Rev. Lett.* **105**, 177001 (2010).
47. Grünhaupt, L. et al. An argon ion beam milling process for native alox layers enabling coherent superconducting contacts. *Appl. Phys. Lett.* **111**, 072601 (2017).
48. Kline, J. S., Wang, H., Oh, S., Martinis, J. M. & Pappas, D. P. Josephson phase qubit circuit for the evaluation of advanced tunnel barrier materials. *Supercond. Sci. Technol.* **22**, 015004 (2008).
49. Masluk, N. A., Pop, I. M., Kamal, A., Mineev, Z. K. & Devoret, M. H. Microwave characterization of josephson junction arrays: Implementing a low loss super-inductance. *Phys. Rev. Lett.* **109**, 137002 (2012).
50. Paik, H. et al. Observation of high coherence in josephson junction qubits measured in a three-dimensional circuit qed architecture. *Phys. Rev. Lett.* **107**, 240501 (2011).
51. Quintana, C. et al. Characterization and reduction of microfabrication-induced decoherence in superconducting quantum circuits. *Appl. Phys. Lett.* **105**, 062601 (2014).
52. Carruzzo, H. M. et al. Distribution of two-level system couplings to strain and electric fields in glasses at low temperatures. *Phys. Rev. B* **104**, 134203 (2021).

ACKNOWLEDGEMENTS

A.B. and J.L. gratefully acknowledge funding by Google LLC. J.L. is grateful for funding from the Deutsche Forschungsgemeinschaft (DFG) for project LI2446/1-2 and for funding from the Baden-Württemberg-Stiftung. We acknowledge support by the KIT-Publication Fund of the Karlsruhe Institute of Technology. We acknowledge support from the German Ministry of Education and Research (BMBF) within the project GeQCoS. A.V.U. acknowledges support from the Russian Science Foundation, project No. 21-72-30026.

AUTHOR CONTRIBUTIONS

The qubit samples were designed by A.B., and fabricated by A.B. with assistance of S. V. Experiments were devised and performed by J.L. in a setup implemented by A.B.

and J.L. A.B. performed E-field simulations and analyzed the data. The manuscript was written by A.B. and J.L. with contributions from A.U.

FUNDING

Open Access funding enabled and organized by Projekt DEAL.

COMPETING INTERESTS

The authors declare no competing interests.

ADDITIONAL INFORMATION

Supplementary information The online version contains supplementary material available at <https://doi.org/10.1038/s41534-022-00532-4>.

Correspondence and requests for materials should be addressed to Alexander Bilmes.

Reprints and permission information is available at <http://www.nature.com/reprints>

Publisher's note Springer Nature remains neutral with regard to jurisdictional claims in published maps and institutional affiliations.



Open Access This article is licensed under a Creative Commons Attribution 4.0 International License, which permits use, sharing, adaptation, distribution and reproduction in any medium or format, as long as you give appropriate credit to the original author(s) and the source, provide a link to the Creative Commons license, and indicate if changes were made. The images or other third party material in this article are included in the article's Creative Commons license, unless indicated otherwise in a credit line to the material. If material is not included in the article's Creative Commons license and your intended use is not permitted by statutory regulation or exceeds the permitted use, you will need to obtain permission directly from the copyright holder. To view a copy of this license, visit <http://creativecommons.org/licenses/by/4.0/>.

© The Author(s) 2022